Synchrotron Radiation News

ISSN: 0894-0886 (Print) 1931-7344 (Online) Journal homepage: https://www.tandfonline.com/loi/gsrn20

High-Energy Adventures at Diamond Light Source

Thomas Connolley, Christine M. Beavers & Philip Chater

To cite this article: Thomas Connolley, Christine M. Beavers & Philip Chater (2020) High-Energy Adventures at Diamond Light Source, Synchrotron Radiation News, 33:6, 31-36, DOI: 10.1080/08940886.2020.1841494

To link to this article: https://doi.org/10.1080/08940886.2020.1841494

High-Energy Adventures at Diamond Light Source

THOMAS CONNOLLEY, CHRISTINE M. BEAVERS, AND PHILIP CHATER
Diamond Light Source, Harwell Science & Innovation Campus, Didcot, Oxfordshire, UK

History and operation of high-energy beamlines at Diamond

Diamond Light Source (DLS), the United Kingdom's national synchrotron facility, is located on the campus of Rutherford Appleton Lab (RAL) in southern Oxfordshire. DLS is jointly funded by the Science and Technology Facilities Council (STFC) within UK Research and Innovation (UKRI) and the Wellcome Trust. Designed as a successor to the ground-breaking Daresbury SRS, Diamond is a third-generation, 3 GeV light source. Construction began in 2003, with beamlines constructed in three phases: Phase I beamlines commenced user operation in 2007 [1, 2], with a further 15 Phase II beamlines completed in 2012. Phase III, completed in 2019, brought the total beamlines to 32. An additional thirty-third beamline, K11 DIAD, was scheduled at press time to start operating in 2020.

The utility of high-energy X-rays to the UK community was established at the SRS, especially for doing *in situ* experiments, such as high-pressure diffraction [3], so a case was made for a Phase I extreme conditions diffraction beamline. This beamline, I15, was designed to offer a high-energy, continuum X-ray spectrum, with white and monochromatic beam, within a generous accessible energy range of 20-80 keV. The X-rays produced by the superconducting wiggler source, if monochromated, can then be focused once to a rugged diffractometer end-station and focused again to the downstream microfocus laser heating end-station [4]. Since first light in 2007, the core I15 experimental modes have solidified such that monochromatic high-energy *in situ* diffraction predominates; the white beam capability is rarely used. The diffractometer is equipped with stages for fine positioning of diamond anvil cells (DACs) [5–7], while also being robust enough to support Paris-Edinburgh cells or a hydraulic p-jump cell [8], as well as systems for applying other *in situ* perturbations, such as a cryostat, strain rigs [9], or electric field devices [10]. The laser heating system on the microfocus end-station is usually engaged in simulating the conditions within the deep earth, but it has also been applied to solid-state physics challenges [11]. Due to I15's high energy range, the beamline is used for conventional powder diffraction as well as an increasing number of total scattering experiments. A selection of beamline and source parameters is given in Table 1.

Beamline I12-JEEP (Joint Engineering, Environmental, and Processing) [14], constructed in Phase 2, is used for imaging, diffraction, and scattering, providing monochromatic photon energies in the range 53-150 keV. Filtered white beam is available, primarily for Energy Dispersive X-Ray Diffraction (EDXD) [15]. It has two experimental hutches, at ~46 m and ~98 m from the source. The beamline is commonly used for time-resolved imaging, tomography, or diffraction experiments. It is possible to sequence monochromatic imaging and diffraction by automated switching of detectors [16]. Sample environments include a uniaxial 100 kN servo-hydraulic mechanical test rig in the second hutch, and a specialized heating cell for *in situ* chemistry experiments [17]. I12 has the space and stage capacity to accept a vast range of sample environments brought by users—two of the more extreme examples are shown in Figure 1 [18]. The hutch flexibility, high photon energy, and flux have given the UK a capability for *in situ*, time-resolved experiments on bulk samples representative of engineering materials, geological samples, or chemical processes. Users have taken full advantage of the beamline for time-resolved imaging of metal solidification [19, 20] and magmas [21]. Diffraction is used for experimental mechanics experiments [22, 23]. Time-resolved diffraction is popular for *in situ* chemistry [24, 25]. The beamline has also found applications in paleontology [26, 27] and the study of osteoporosis and fracture in bulk bone samples [28, 29]. Other notable advances enabled by the beamline are understanding and minimizing catastrophic failure modes in commercial Li-ion batteries [30] and the study of molten metal flow during welding [31].

The third high-energy instrument, I15-1, is the dedicated X-ray Pair Distribution Function (XPDF) beamline. I15-1 utilizes an inboard slice of the horizontal fan from I15's wiggler source, allowing independent, simultaneous operation of both beamlines. I15-1 achieves the high-energy, high-flux data collections required for quality XPDF data using a cryo-cooled bent-Laue monochromator [32] and a vertically focussing multi-layer mirror [33]. The end-station has been optimized to give a low background signal. I15-1 typically operates with two large area detectors, one placed close to the sample to the provide the large Q range required for high-quality total scattering and XPDF data (Q_{max} up to 40 Å^{-1} at 76.7 keV), and one mounted further from the sample for simultaneous higher-resolution Bragg diffraction data. High-energy XPDF data collections on I15-1 allow researchers to study the local structure of crystalline, semi-crystalline, and amorphous solids and liquids with a speed and robustness that had not been possible at DLS before. I15-1 has attracted a diverse range of scientific fields, such as solvation of nanoparticles [34], porous liquids [35] and gasses [36], ferroelectrics [37], catalysts [38], and batteries [39].

Table 1: Summary of the Diamond high-energy beamlines and their wigglers.

Beamline	Monochromated photon energy range	White beam available	Beam size at sample position (h x v)	Wiggler peak field	Wiggler total length
I12	53-150 keV	Yes, with variable filtration	No focusing. Collimated by slits from 30 µm x 30 µm up to 95 mm x 30 mm	4.2T	1.2m [12]
I15	20-80 keV	Yes	115 µm x 76 µm primary focus; 9 µm x 5 µm in micro-focus mode	3.5T	1.5m [13]
I15-1	40.0, 65.4 and 76.6 keV	No	Focused: 700 µm horizontal by 10 µm vertical. Standard size at sample 700 µm x 150 µm		

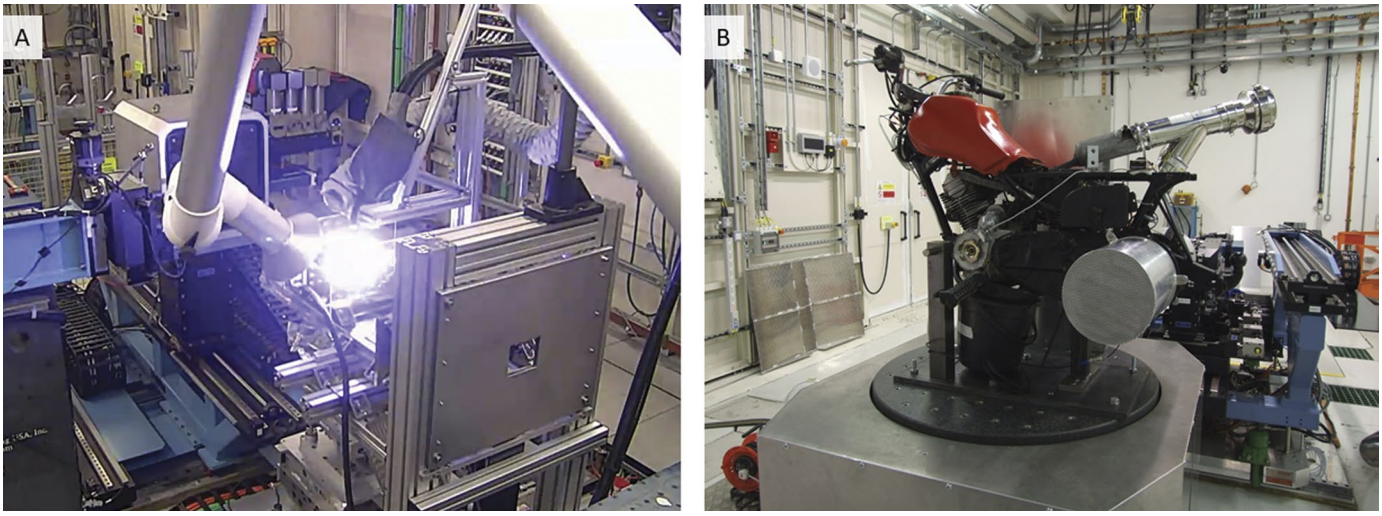

Figure 1: Two examples of large sample environments that can be accommodated by I12's end-stations: (A) a wire arc additive manufacturing(WAAM) system; (B) a motorbike engine.

Due to Diamond's location on the Rutherford Appleton Laboratory campus, beamline experimentalists can also benefit from the ISIS Neutron and Muon Source, just a short walk away. Neutrons and high-energy X-rays are both well-suited to *in situ* and *in operando* studies; the speed of X-ray techniques can benefit from the elemental sensitivity and penetration depth of neutrons. It is possible to apply use of both Diamond and ISIS in a single proposal if the complementarity of X-rays and neutrons is necessary to the aims of the experiment. In the case of PDF measurements, users collecting neutron PDF data at ISIS will automatically be approved for equivalent XPDF data collections on I15-1.

Science and instrumentation highlights

On I15, simultaneous high-pressure, high-temperature (HPHT) experiments are often used to simulate geophysical, chemical, and industrial processes. There are two methods used to raise the temperature in a DAC: resistive heating and laser heating [40]. IR laser heating is the premier method of achieving temperatures from 1000°C to beyond 3000°C and has been successfully implemented on I15 [4]. Resistive heating, which is used to span the region from room temperatures to 1000°C, can be further subdivided into internal and external resistive heating; external indicates that the entire DAC assembly is heated, while internal requires placement of a heating element within the DAC. External resistive heating is relatively trivial and commercially available products exist; unfortunately, they are limited in their temperature range to ~700°C, unless the entire apparatus is placed under vacuum. Internally heated designs are capable of higher temperatures, up to 1100°C, but due to the miniaturization required to place the heaters near the sample, this technique is generally limited to experts. An in-

ternal resistively heated DAC that bridges the temperature gap between techniques and is user-friendly has been a known need within the high-pressure community; the HXD95 DAC, shown in Figure 2A, has been designed to meet these needs.

Another challenge in simultaneous HTHP experimentation is that many of the systems of interest at temperatures ranging from 700-1100°C and moderate pressures (≤ 5 GPa) involve melts. An understanding of the atomic structure of amorphous materials requires access to the pair distribution function (PDF), which is denoted G(r). The resolution achievable in G(r) is dependent on the maximum scattering angle measured in the diffraction data. Often, the opening angle of a DAC is too limiting to measure high-angle, high-Q data. High-energy X-rays, combined with the HXD95 DAC, which was designed with a large angular opening, permit the collection of high-Q simultaneous HPHT diffraction data. A recent exploration of the phase behavior of gallium was concluded [41]. Gallium is known to form Ga_2 dimers in the solid state at ambient temperatures and pressures, but these dimers were not observed in the liquid state at any pressure or temperature. Various coordination environments of gallium within the liquid phase were simulated, and their representative populations within the melt were determined using Reverse Monte Carlo (RMC) fitting. This level of detail on the constituents within the gallium melt gives insight into its complicated solid-state behavior. The HXD95 DAC allowed good quality scattering data, shown in Figure 2B, to be collected at higher Q, which improves the real space resolution [42]; in more complicated multi-element systems, this could be critical to resolving structural details.

A specific feature of I12 JEEP is the space available for user-owned sample environments. UK research groups have taken advantage of this capability by installing equipment for the *in situ* study of additive manufacturing. Commonly known as "3D printing," additive manufacturing encompasses a number of techniques for producing components in a range of materials. In the case of metals, the main additive manufacturing techniques involve controlled melting and deposition of a feedstock such as a powder or wire. Laser additive manufacturing (LAM) uses a high-energy laser beam to melt powder particles into a solid structure in under 1/1000th of a second. The speed of the laser-material interaction makes it difficult to optimize processing conditions, resulting in defects. Concern about the impact of defects hinders the adoption of LAM as a manufacturing process for high-value, safety-critical components, such as aerospace parts and biomedical devices. Leung et al. [43] used X-ray imaging at 5100 frames/second to study the formation and evolution of melt tracks, porosity, spatter and denuded zones during LAM of gas atomized Invar 36 powder. A sample of the experimental images is given in Figure 3. Quantification of pore and spatter movements determined crucial information about their velocities and direction, which is not possible to acquire using other techniques. It was found that Marangoni convection dominated the liquid metal flow, reaching a velocity of 400 mm s^{-1}. A further study looked at the effect of powder oxidation on defect formation [44].

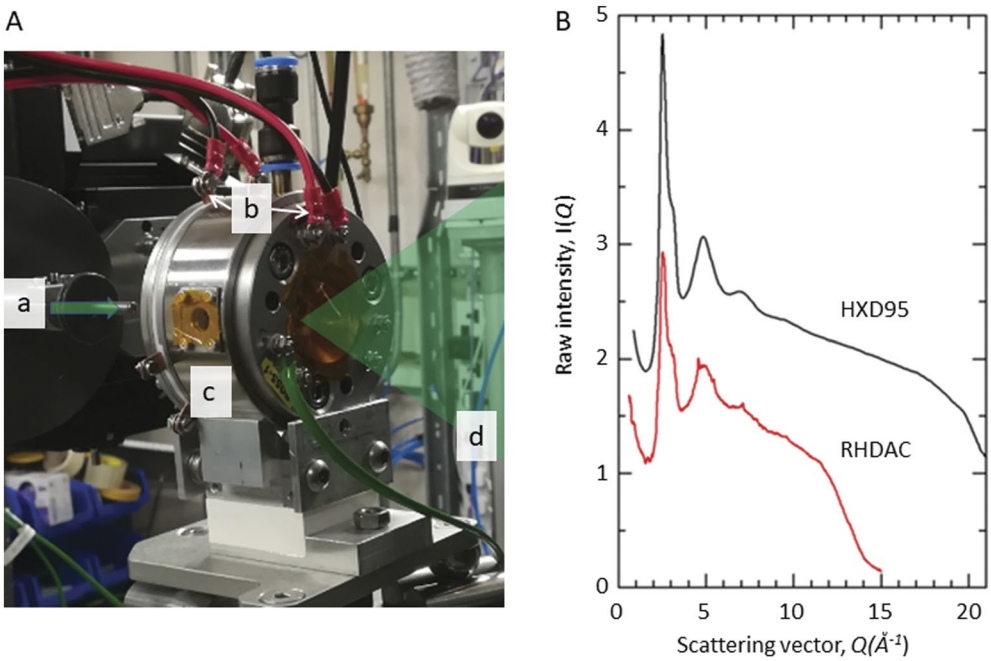

Figure 2: (A) An image of the HXD95 DAC on the I15 diffractometer station, annotated as follows: (a) X-ray pinhole and green arrow indicating X-ray beam direction; (b) DC power connectors; (c) water-cooled gas confinement ring; (d) green cone indicating diffracted X-rays. (B) A comparison of scattering data from gallium in the HXD95 versus an external resistively heated DAC (RHDAC). For clarity, the HXD95 data has been displaced vertically. Both images adapted from [42].

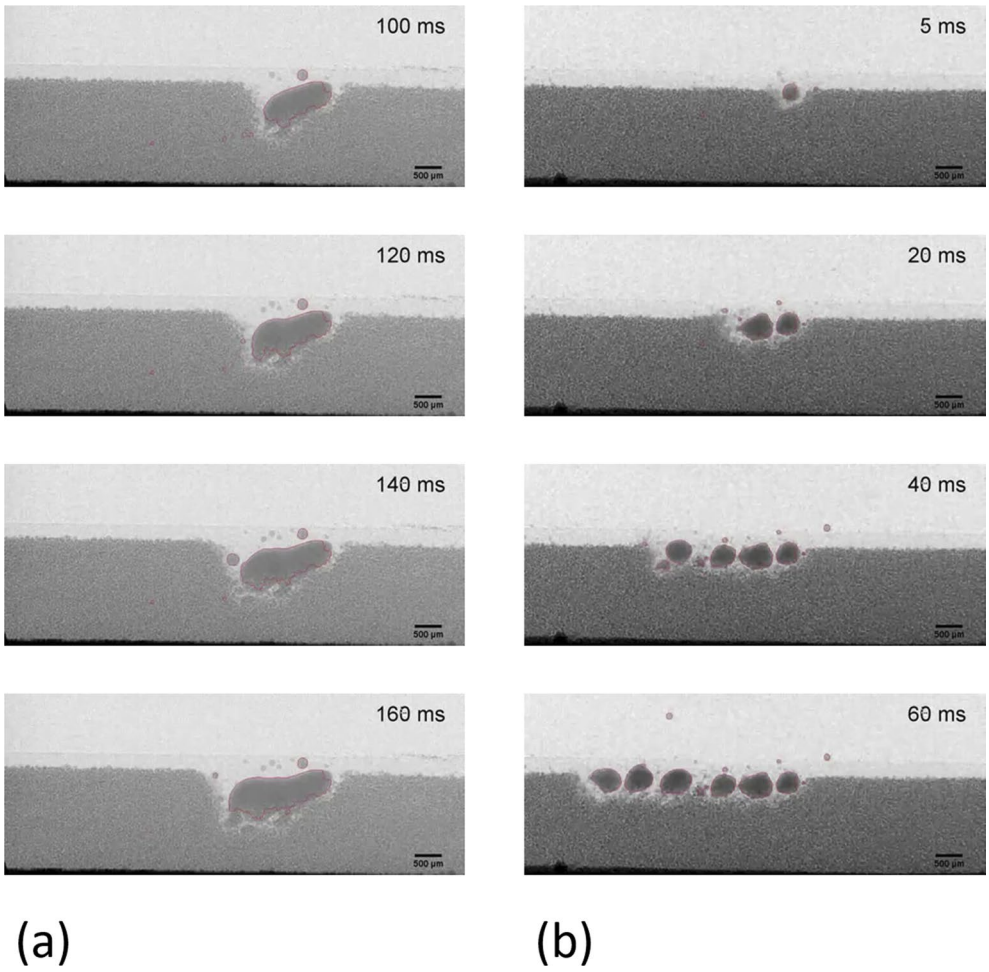

Figure 3: X-ray video stills from laser additive manufacturing (LAM) experiment showing (a) continuous melt track formation; (b) formation of disconnected melt beads. Adapted from videos generated during the work published in [43] under a Creative Commons Attribution 4.0 International License.

A different type of metal additive manufacturing is Wire Arc Additive Manufacturing (WAAM). A robotically controlled electric arc welding torch is used to melt a metallic feed wire and deposit it, layer by layer, to form a finished component (Figure 1A). The advantage of WAAM is it can be used to form large components over one meter in extent. During WAAM and welding, metallic alloys undergo rapid transitions in state between liquid and solid. Fluid flow inside the pool of molten metal significantly influences the properties of the manufactured component. I12's high-speed, high-energy radiography capability was employed to observe melt pool formation and flow dynamics in steels [31]. Theorized differences between fusion zone shapes for low- and high-S steels, previously observed by *ex situ* microscopy of welds, could be observed directly during WAAM. By using tracer particles of W or Ta, researchers were able to quantify flow velocities within the melt pool. These novel experimental observations enhanced understanding of how melt pools form and evolve under realistic fusion welding conditions.

A recent development on beamline I15-1 is the Diamond Radial *In situ* X-ray (DRIX) electrochemical cell [45], improving on previous radial-geometry electrochemical cells [46–48]. In radial geometry, the X-ray beam travels perpendicular to the cell stacking direction. The narrow vertical beam profile of I15-1, provided by the vertically focussing multi-layer mirror (down to 9 µm FWHM), allows an individual layer of the cell (e.g., the anode or cathode of interest) to be studied in isolation. The DRIX cell (Figure 4a) can be easily assembled inside a glove box and provides the low, repeatable background necessary for quality XPDF data. A range of low-Z current collectors are available which reduce attenuation of the scattered signal; these are made of Al, Cu-coated PEEK, or vitreous carbon and can be selected based on chemical compatibility of the system being studied. On the I15-1 beamline, up to 10 DRIX cells can be mounted on the sample stage using a multi-cell mount that provides some alignment of the cells and facilitates cable management. An 8-channel potentiostat (Ivium n-Stat) is available and has been

integrated into the beamline control software, so that up to eight cells can be cycled simultaneously with XPDF data collected at regular intervals.

DRIX cells have been applied to the study of a range of battery materials, including nanostructured high-capacity cathode material $Li_4Mn_2O_5$ [43]. This material adopts a disordered rock salt structure, with Li and Mn on the same crystallographic site and 1/6 oxygen vacancies. The mechanochemical alloying used to synthesize nanostructured $Li_4Mn_2O_5$ gives rise to very broad Bragg peaks and a high concentration of defects, making traditional crystallographic analyses of limited use. The relatively light elements present make full characterisation with X-rays a significant challenge. Using the DRIX cell, it was possible to collect quality XPDF data in only a few minutes, allowing the average and local structure to be tracked *in situ* during electrochemical cycling (Figure 4b and c) [45]. Upon charging, nanostructured $Li_4Mn_2O_5$ evolves via a solid-solution behavior with the disordered rock-salt structure maintained throughout, despite losing a total of 75% of Li (50% of all cations). The XPDF data were able to rule out any phase transformations, which can be unfavorable for battery longevity, showing instead a gradual breathing of the Mn lattice, which correlates with the electrochemistry. At high states of charge, weak diffuse signals were observed, which were assigned to a short-range-ordered superstructure of partial cation-layer ordering.

Future developments

To maintain competitiveness, DLS runs a rolling program of beamline upgrades, including new detectors better optimized for high-energy operation and new sample environments. I15-1 is constructing a bespoke "Angularly-Resolved CdTe" (ARC) detector, which will be installed in Summer 2021. It has 55-µm-pixel-size photon-counting sensors capable of detecting high-energy X-rays with high efficiency [49]. This 4.7-megapixel detector has an angular coverage of 100°, giving access to a wide *Q* coverage even at I15-1's lowest operating energy of 40 keV. At press time, I15 was planned to take delivery of a Dectris 2M Pilatus3 X with CdTe sensors in late 2020, which will be a step change in high-energy X-ray detection efficiency and speed from current detectors. In the same time period, I12 was scheduled to receive a new uniaxial 10 kN loading rig for tomography experiments, which will be upgraded later with an IR furnace and sample cells enabling *in situ* heating and tensile/compressive loading in inert gas or vacuum.

Most synchrotrons worldwide are undergoing or exploring high-brightness, low-emittance upgrades. The fourth-generation, diffraction-limited storage ring plan for DLS is well underway. The Diamond-II Science Case and Conceptual Design Review proposed a machine lattice based on Double Triple Bend Achromats (DTBAs). This design yields an increase in brightness and coherence by a factor of up to 70 and provides mid-section straights so that existing bending magnet beamlines could use insertion devices. It is expected that there will be five extra straight sections available for new insertion device beamlines. The design increases the electron beam energy from 3.0 to 3.5 GeV, providing greatly increased photon flux at higher energies. The use of Cryogenic Permanent Magnet Undulator (CPMU) or Superconducting Undulator (SCU) insertion devices will give the potential for some instruments to operate at 40-45 keV. A low-divergence, high-energy, micro or nanofocus diffraction beamline was outlined in the Diamond-II Science Case and is currently being explored in further detail. I15, I15-1, and I12 are expected to retain their wiggler sources and will see 2-6 times increases in flux at the higher ends of their respective spectrums, as well as a decrease in vertical divergence. These flux gains will benefit *in situ* studies and enable better time resolution.

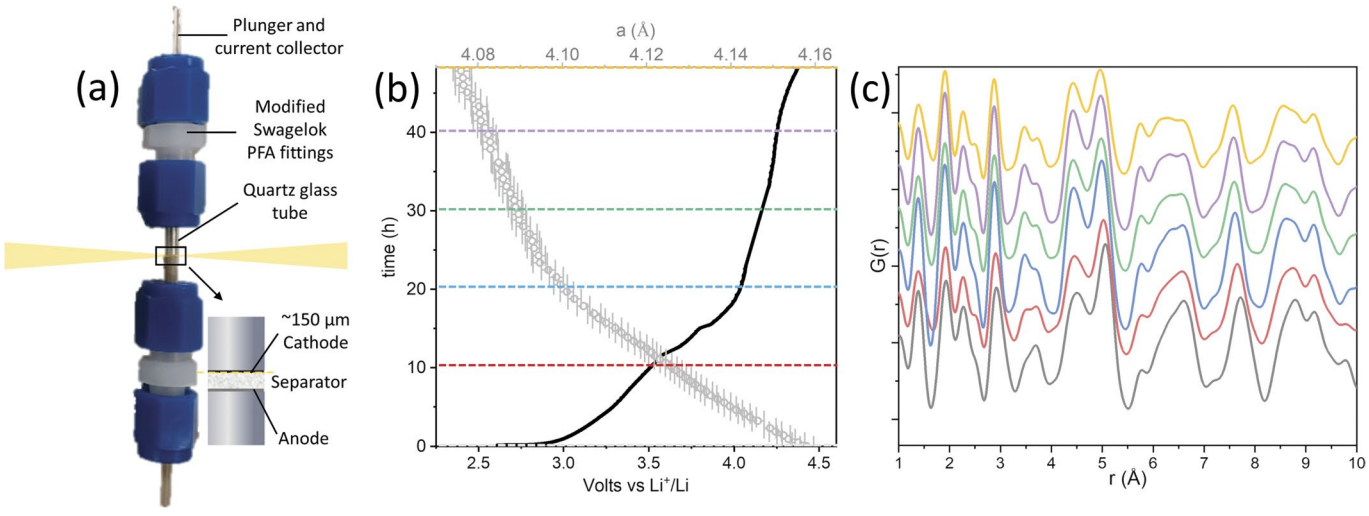

Figure 4: (a) Labelled drawing of an assembled DRIX cell with a schematic representation of a cell stack shown inset. The incoming and transmitted X-ray beams are represented in yellow. (b) Electrochemical performance (solid line) overlaid with refined lattice parameter (empty circles) of nanostructured $Li_4Mn_2O_5$. The colored lines in (b) reflect the selected XPDF datasets shown in (c).

Acknowledgments

We acknowledge the support of the beamline staff who have contributed significantly to the developments mentioned in this work, namely Michael Drakopoulos, Robert Atwood, Oxana Magdysyuk, Stefan Michalik, Bob Humphreys, Heribert Wilhelm, Dean S. Keeble, Maria Diaz-Lopez, Geoffrey L. Cutts, Allan Ross, Annette Kleppe, Dominik Daisenberger, Simone Anzellini, and Volodymyr Khotkevych. ■

References

1. R. Walker, *4th Asian Particle Accelerator Conference*, 66-70 (2007).
2. R. Bartolini, *IEEE Particle Acclerator Conference (PAC) 07*, (2007).
3. R. J. Nelmes and M. I. McMahon, *Journal of Synchrotron Radiation* **1**(1), 69–73 (1994). DOI: 10.1107/S0909049594006679.
4. S. Anzellini et al., *Journal of Synchrotron Radiation* **25**(6), 1860–1868 (2018). DOI: 10.1107/S1600577518013383.
5. R. N. Widmer et al., *Journal of the American Chemical Society* **141**(23), 9330–9337 (2019). DOI: 10.1021/jacs.9b03234.
6. S. E. Finnegan et al., *Physical Review B* **101**(17), 174109 (2020). DOI: 10.1103/PhysRevB.101.174109.
7. H. Breton et al., *American Mineralogist* **104**(12), 1781–1787 (2019). DOI: 10.2138/am-2019-7065.
8. N. J. Brooks et al., R*eview of Scientific Instruments* **81**(6), 064103 (2010). DOI: 10.1063/1.3449332.
9. L. C. D. Fielding et al., *Acta Materialia* **105**, 52–58 (2016). DOI: 10.1016/j.actamat.2015.11.029.
10. G. Wang et al., *Journal of Materials Chemistry A* **7**(37), 21254–21263 (2019). DOI: 10.1039/C9TA07904A.
11. S. Anzellini et al., *Scientific Reports* **9**(1), 13034 (2019). DOI: 10.1038/s41598-019-49676-y.
12. Z. Pate, et al., *International Particle Accelerator Conference* (2017).
13. S. Khrushchev et al., *RuPAC 2006*, 398–400 (2006).
14. M. Drakopoulos et al., *Journal of Synchrotron Radiation* **22**(3), 828–838 (2015). DOI: 10.1107/S1600577515003513.
15. A. M. Korsunsky et al., *Materials Letters* **64**(15), 1724–1727 (2010).
16. C. A. Stitt et al., *Scientific Reports* **7**(1), 7999 (2017). DOI: 10.1038/s41598-017-08601-x.
17. S. J. Moorhouse et al., *Review of Scientific Instruments* **83**(8), 084101 (2012). DOI: 10.1063/1.4746382.
18. N. Baimpas et al., *Journal of Synchrotron Radiation* **20**(2), 316–323 (2013).
19. B. Cai et al., *Acta Materialia* **196**, 200–209 (2020). DOI: 10.1016/j.actamat.2020.06.041.
20. S. Karagadde et al., *Nat Commun* **6** (2015). DOI: 10.1038/ncomms9300.
21. F. Arzilli et al., *Nature Geoscience* **12**(12), 1023–1028 (2019). DOI: 10.1038/s41561-019-0468-6.
22. A. Reid et al., *Tribology International* **140**, 105893 (2019). DOI: 10.1016/j.triboint.2019.105893.
23. T. J. Marrow et al., *Carbon* **96**, 285–302 (2016). DOI: 10.1016/j.carbon.2015.09.058.
24. Y. Pang et al., *Journal of Applied Crystallography* **52**(6), 1264–1270 (2019). DOI: 10.1107/S1600576719012500.
25. Y. Wu et al., *Angewandte Chemie International Edition* **55**(45), 14081–14084 (2016). DOI: 10.1002/anie.201608463.
26. C. Baars, M. Ghobadi Pour, and R. C. Atwood, *Geological Magazine* **150**(02), 371–380 (2013). DOI: 10.1017/S0016756812000829.
27. R. J. Garwood et al., *Proceedings of the Royal Society B: Biological Sciences* **283**(1827), 20160125 (2016). DOI: 10.1098/rspb.2016.0125.
28. S. Ma et al., *Scientific Reports* **7**(1), 43399 (2017). DOI: 10.1038/srep43399.
29. L. Yan et al., *Journal of the Mechanical Behavior of Biomedical Materials* **109**,103838 (2020). DOI: 10.1016/j.jmbbm.2020.103838.
30. D. P. Finegan et al., *Energy & Environmental Science* **10**(6), 1377–1388 (2017). DOI: 10.1039/C7EE00385D.
31. L. Aucott et al., *Nature Communications* **9**(1), 5414 (2018). DOI: 10.1038/s41467-018-07900-9.
32. J. P. Sutter et al., *AIP Conference Proceedings* **1741**(1), 040005 (2016). doi:10.1063/1.4952877
33. J. P. Sutter et al., *Optics Express* **27**(11), 16121–16142 (2019). DOI: 10.1364/OE.27.016121.
34. S. L. J. Thomä et al., *Nature Communications* **10**(1), 995 (2019). DOI: 10.1038/s41467-019-09007-1.
35. R. Gaillac et al., *Nature Materials* **16**(11), 1149–1154 (2017). DOI: 10.1038/nmat4998.
36. C. Zhou et al., *Nature Communications* **9**(1), 5042 (2018). DOI: 10.1038/s41467-018-07532-z.
37. I. Levin et al., *Chemistry of Materials* **31**(7), 2450–2458 (2019). DOI: 10.1021/acs.chemmater.8b05187.
38. T. Chen et al., *Journal of the American Chemical Society* **141**(50), 19616–19624 (2019). DOI: 10.1021/jacs.9b06120.
39. M. Diaz-Lopez et al., *Advanced Energy Materials* **10**(7), 1902788 (2020). doi:10.1002/aenm.201902788
40. S. Anzellini and S. Boccato, *Crystals* **10**(6), 459 (2020).
41. J. W. E. Drewitt et al., *Physical Review Letters* **124**(14), 145501 (2020). DOI: 10.1103/PhysRevLett.124.145501.
42. M. Louvel et al., *Journal of Synchrotron Radiation* **27**(2), 529–537 (2020). DOI: 10.1107/S1600577519016801.
43. C. L. A. Leung et al., *Nature Communications* **9**(1), 1355 (2018). DOI: 10.1038/s41467-018-03734-7.
44. C. L. A. Leung et al., *Acta Materialia* **166**, 294–305 (2019). DOI: 10.1016/j.actamat.2018.12.027.
45. M. Diaz-Lopez et al., *Journal of Synchrotron Radiation* **27**(5) (2020). DOI: 10.1107/S160057752000747X.
46. J. M. Stratford et al., *Journal of the American Chemical Society* **139**(21), 7273–7286 (2017). DOI: 10.1021/jacs.7b01398.
47. H. Liu et al., *Journal of Applied Crystallography* **49**(5), 1665–1673 (2016). DOI: 10.1107/S1600576716012632.
48. M. J. Young et al., *Journal of Synchrotron Radiation* **24**(4), 787–795 (2017). DOI: 10.1107/S1600577517006282.
49. E. N. Gimenez et al., *2019 IEEE Nuclear Science Symposium and Medical Imaging Conference (NSS/MIC)* (2019).